

# Three-Dimensional Simulation of Double-Detonations in the Double-Degenerate Model for Type Ia Supernovae and Interaction of Ejecta with a Surviving White Dwarf Companion

ATARU TANIKAWA,<sup>1,2</sup> KEN'ICHI NOMOTO,<sup>3</sup> AND NAOHITO NAKASATO<sup>4</sup>

<sup>1</sup>*Department of Earth Science and Astronomy, College of Arts and Sciences, The University of Tokyo, 3-8-1 Komaba, Meguro-ku, Tokyo 153-8902, Japan; tanikawa@ea.c.u-tokyo.ac.jp*

<sup>2</sup>*RIKEN Center for Computational Science, 7-1-26 Minatojima-minami-machi, Chuo-ku, Kobe, Hyogo 650-0047, Japan*

<sup>3</sup>*Kavli Institute for the Physics and Mathematics of the Universe (WPI), The University of Tokyo, 5-1-5, Kashiwanoha, Kashiwa, 277-8583, Japan*

<sup>4</sup>*Department of Computer Science and Engineering, University of Aizu, Tsuruga Ikki-machi Aizu-Wakamatsu, Fukushima, 965-8580, Japan*

## ABSTRACT

We study the hydrodynamics and nucleosynthesis in the double-detonation model of Type Ia supernovae (SNe Ia) and the interaction between the ejecta and a surviving white dwarf (WD) companion in the double-degenerate scenario. We set up a binary star system with  $1.0M_{\odot}$  and  $0.6M_{\odot}$  carbon-oxygen (CO) WDs, where the primary WD consists of a CO core and helium (He) shell with  $0.95$  and  $0.05M_{\odot}$ , respectively. We follow the evolution of the binary star system from the initiation of a He detonation, ignition and propagation of a CO detonation, and the interaction of SN ejecta with the companion WD. The companion (or surviving) WD gets a flung-away velocity of  $\sim 1700 \text{ km s}^{-1}$ , and captures  $^{56}\text{Ni}$  of  $\sim 0.03M_{\odot}$ , and He of  $3 \times 10^{-4}M_{\odot}$ . Such He can be detected on the surface of surviving WDs. The SN ejecta contains a “companion-origin stream”, and unburned materials stripped from the companion WD ( $\sim 3 \cdot 10^{-3}M_{\odot}$ ), although the stream compositions would depend on the He shell mass of the companion WD. The ejecta has also a velocity shift of  $\sim 1000 \text{ km s}^{-1}$  due to the binary motion of the exploding primary WD. These features would be prominent in nebular-phase spectra of oxygen emission lines from the unburned materials like SN 2010lp and iPTF14atg, and of blue- or red-shifted Fe-group emission lines from the velocity shift like a part of sub-luminous SNe Ia. We expect SN Ia counterparts to the D<sup>6</sup> model would leave these fingerprints for SN Ia observations.

*Keywords:* binaries: close — galaxies: evolution — hydrodynamics — supernovae: general — white dwarfs

## 1. INTRODUCTION

The progenitor system of Type Ia supernovae (SNe Ia) is one of the biggest mysteries in astronomy and astrophysics. It is generally thought that an SN Ia is powered by thermonuclear explosion of a carbon-oxygen (CO) white dwarf (WD). However, the progenitor system is yet to be confirmed. Since a single CO WD never starts exploding spontaneously, an exploding CO WD must have a companion star. The stellar type of the companion star has been under debate. There is a famous and long-standing dichotomy between single degenerate (SD; e.g. Nomoto & Leung 2018) and double degenerate (DD

Iben & Tutukov 1984; Webbink 1984) scenarios, where the companion star is a main-sequence or red-giant star in the SD scenario, or is another WD in the DD scenario. Other scenarios are also suggested, such as the core degenerate scenario (Kashi & Soker 2011).

Recent observations have revealed some significant constraints on the SD scenario. Red-giant stars are absent in the pre-explosion images of SN 2011fe and SN 2014J (Li et al. 2011; Kelly et al. 2014, respectively), which are the closest SNe Ia in these decades. No main-sequence star has been detected in a supernova remnant LMC SNR 0509-67.5 (Schaefer & Pagnotta 2012; Litke et al. 2017), although spin-up/spin-down models can explain the non-detection (Justham 2011; Di Stefano et al. 2011; Hachisu et al. 2012; Benvenuto et al. 2015). However, we should note some SNe Ia indicate signals supporting the SD scenario. For example, PTF11kx has

given a signature of the interaction of supernova (SN) ejecta and circumstellar matter (Dilday et al. 2012), and iPTF14atg and SN 2012cg exhibit the interaction of SN ejecta and non-degenerate companion stars (Cao et al. 2015; Marion et al. 2016, respectively), although for iPTF14atg and SN 2012cg these detections have been contested (e.g. Kromer et al. 2016; Shappee et al. 2018, respectively). SNe Ia may have several types of progenitor systems, although they may be dominated by a single type of a progenitor system.

The DD scenario suffers from the following problem, if one assumes the DD systems are dominant progenitor systems for SNe Ia. Super-Chandrasekhar DD systems, whose total mass is more than Chandrasekhar mass, merge at a fewer rate than the SN Ia event rate (e.g. Maoz et al. 2014). In the violent merger model (Pakmor et al. 2010), the primary CO WD in a DD system is ignited by hydrodynamical effects, and hence super-Chandrasekhar DD systems is not necessarily needed. However, Sato et al. (2015, 2016) have shown that the violent merger model works well only when DD systems have the companion mass of  $\gtrsim 0.8M_{\odot}$ ; the DD systems are super-Chandrasekhar DD systems. Although Kashyap et al. (2015, 2017) have suggested spiral instability after DD mergers drives thermonuclear explosions, Sato et al.’s results have indicated the spiral instability can apply only to super-Chandrasekhar DD systems. Fenn et al. (2016) have numerically demonstrated thermonuclear explosion of the primary WDs in detached DD systems, and found that the successful DD systems are super-Chandrasekhar DD systems. Another solution could be collisional DD models (Raskin et al. 2009; Rosswog et al. 2009; Lorén-Aguilar et al. 2010; Dong et al. 2015). Katz & Dong (2012) have argued DD collisions in triple systems can account most of SNe Ia, but it has been controversial (Maoz et al. 2014).

If we take into account sub-Chandrasekhar DD systems, whose total mass is less than the Chandrasekhar mass, the total merger rate of super- and sub-Chandrasekhar DD systems would be comparable to the SN Ia event rate. Such DD systems may explode as SNe Ia with the aid of helium (He) ignition – the double detonation model.

Originally, the double detonation model has been suggested as a derivative of the SD scenario, since the companion star is a non-degenerate star, such as a He star (Nomoto 1982; Woosley et al. 1986; Livne 1990; Livne & Glasner 1990). Guillochon et al. (2010) and Pakmor et al. (2013) have shown that the primary CO WD in a DD system can possibly experience CO detonation driven by He detonation. In particular, a DD system in Guillochon et al. (2010) is a sub-Chandrasekhar DD

system. The double detonation model in DD systems requires only a small amount of He,  $\lesssim 0.01M_{\odot}$ , since the He detonation is triggered by hydrodynamical effects of shock compression. This model is called “Dynamically Driven Double-Degenerate Double-detonation ( $D^6$ ) model” by Shen et al. (2018), or “helium-ignited violent merger model” by Pakmor et al. (2013). Hereafter, we refer to this model as  $D^6$  model for simplicity. The  $D^6$  model is more advantageous than the double detonation model in SD systems in the following reason. Since the double detonation model in SD systems requires such a large amount of He as  $\gtrsim 0.1M_{\odot}$  (Nomoto 1982), this model is predicted to leave behind signature of the He detonation (Woosley & Weaver 1994; Woosley & Kasen 2011); actually the signature has been found (Jiang et al. 2017; Maeda et al. 2018), although the observations of such signature has been rare.

The distinct point of the  $D^6$  model from other DD models is that the companion WD can survive thermonuclear explosion of the primary WD (Pakmor et al. 2013). The DD system is so close that the surviving WD gets hypervelocity (HV)  $\gtrsim 10^3$  km after the primary WD explodes. Recently, Shen et al. (2018) have found out three HV WDs from Gaia DR2. If the  $D^6$  model can explain all the SNe Ia in the Milky Way Galaxy, one should find  $\sim 30$  HV WDs within 1 kpc of the Sun. The number of HV WDs are fewer than expected. However, if more HV WDs would be found in near future, it would support the statement that the  $D^6$  model is a major origin of SNe Ia.

If the  $D^6$  model would be the case for a significant fraction of SNe Ia, it is important to study SN ejecta and surviving WD of the  $D^6$  model. Guillochon et al. (2010) and Pakmor et al. (2013) have not followed WD explosion although they have investigated the merging process of DD systems, and He detonation. Papish et al. (2015) have focused only on ejecta-companion interaction, manually setting up the blast wave of SN Ia explosion. There are several studies for the interaction of SN ejecta with non-degenerate companions (e.g. Pakmor et al. 2008; Liu et al. 2012, 2013).

Therefore, we numerically follow the following sequence of events: the He detonation, CO detonation, WD explosion, and ejecta-companion interaction by means of Smoothed Particle Hydrodynamics (SPH) simulation coupled with nuclear reactions. Although we treat super-Chandrasekhar DD system, we believe super- and sub-Chandrasekhar DD systems have common features in the  $D^6$  explosion.

Our paper is structured as follows. In section 2, we present our SPH simulation method and initial conditions. In section 3, we show simulation results. In

section 4, we compare our results with observations of SNe Ia and HV WDs. In section 5, we summarize this paper.

## 2. METHOD

Our SPH code is the same as used in Tanikawa et al. (2017) (see also Kawana et al. 2018; Tanikawa 2018a,b). We thus briefly describe our code. For equation of state (EoS), we use Helmholtz EoS without Coulomb corrections (Timmes & Swesty 2000). We couple our SPH code with nuclear reaction networks Aprox13 (Timmes et al. 2000). We optimize our code on massively parallel computing environments utilizing FDPS (Iwasawa et al. 2016; Namekata et al. 2018), and accelerate calculations of particle-particle interactions with AVX/AVX2/AVX512 instructions (e.g. Tanikawa et al. 2012, 2013).

Our initial condition is a binary star system consisting of  $1.0M_{\odot}$  and  $0.6M_{\odot}$  WDs. The primary one has a CO core and a He shell with  $0.95M_{\odot}$  and  $0.05M_{\odot}$ , respectively, and the companion one has only a CO core. In our setup, the companion WD has no He shell. This is because we assume that its He shell transfers to the primary WD through the prior merging process. Nevertheless, this is an extreme case. Moreover, He shell masses on primary and companion WDs depend on details of the He star evolution and mass transfer, i.e. binary parameters of progenitors (Iben & Tutukov 1985; Iben et al. 1987; Kawai et al. 1988; Iben & Tutukov 1991; Zenati et al. 2018). In future, we will investigate cases where primary and companion WDs have various total and He shell masses.

We set up the initial condition as follows. We make a single CO WD in the same way as Tanikawa et al. (2015) (see also Sato et al. 2015, 2016). We map SPH particles consistently with the 1D profile of a fully degenerate CO WD with  $10^6$  K, where the mass fractions of carbon and oxygen are  $X_{\text{C}} = 0.5$  and  $X_{\text{O}} = 0.5$ , respectively. Subsequently, we relax a configuration of SPH particles by evolving these SPH particles by our SPH code. Since this relaxation involves dissipative process, temperature of SPH particles is increased up to several  $10^6$  K. For the primary WD, we change the CO composition of SPH particles in the outermost shell with  $0.05M_{\odot}$  to the mass fractions of helium, carbon, and oxygen of  $X_{\text{He}} = 0.6$ ,  $X_{\text{C}} = 0.2$ , and  $X_{\text{O}} = 0.2$ , respectively. Thus, the He shell contains  $0.03M_{\odot}$  of helium. Note that He and C+O can be mixed in the merging process of two WDs due to Kelvin-Helmholtz instability (Pakmor et al. 2013). The mixing of He and C+O facilitates ignition and propagation of He detonation (Shen & Moore 2014). Since we do not smooth chemical elements in our SPH code,

we cannot follow the mixing of chemical compositions along with the Kelvin-Helmholtz instability. This is because we do not begin our simulation from the merging process.

We put these two WDs so that they orbit around each other on a circular orbit with a semi-major axis of  $1.6 \cdot 10^4$  km, where the Roche-lobe radius of the companion WD is the same as its radius according to an approximate formula of Eggleton (1983). We assign star ID 1 and 2 to SPH particles initially belonging to the primary and companion WDs, respectively. We put a hotspot with a size of  $10^3$  km in the He shell of the primary WD. The hotspot is located at the orbital plane of the binary star system in the propagating direction of the primary WD. We set such a large hotspot in order to initiate a He detonation easily.

The total number of SPH particles is 67, 108, 864. The primary and companion WDs consist of 41, 943, 040 and 25, 165, 824 SPH particles, respectively. All the particles have equal mass. This means the mass resolution is  $\sim 2.4 \cdot 10^{-8}M_{\odot}$ . We call this mass resolution “fiducial mass resolution”.

For resolution check, we perform an additional simulation in the following initial condition. We prepare the same WD as the primary WD described above, except that the mass resolution is 2 times higher. Therefore, the number of SPH particles for the WD is 83, 886, 080, and the mass resolution is  $\sim 1.2 \cdot 10^{-8}M_{\odot}$ . We call this mass resolution “higher mass resolution”.

In section 3, we treat two coordinate systems: Cartesian and spherical coordinate systems. In the Cartesian coordinate system, the barycenter of the binary star system is at the coordinate origin, and the barycentric velocity is zero. The orbital plane of the binary star system is set to the  $x$ - $y$  plane. At the initial time, the centers of the primary and companion WDs sit on the  $x$ - and  $y$ -axes, respectively. The angular momentum vector of the binary star system points in the same direction of the  $z$ -axis. To coordinate transformation between the Cartesian and spherical coordinate systems,  $x = r \cos \phi \sin \theta$ ,  $y = r \sin \phi \sin \theta$ , and  $z = r \cos \theta$ , where  $r = (x^2 + y^2 + z^2)^{1/2}$ , and  $\theta$  and  $\phi$  are the polar and azimuthal angles, respectively.

## 3. RESULTS

We first overview our simulation results in section 3.1. We investigate the SN ejecta and surviving WD (or companion WD) in detail in sections 3.2 and 3.3, respectively.

### 3.1. Overview

Figure 1 shows the time evolution of the density distribution in the binary star system. He detonation starts

in the He shell of the primary WD at the time  $t = 0$  s, and propagates in the He shell, not into the CO core of the primary WD. The He detonation converges on the back side of the primary WD from its beginning point at  $t \sim 1.25$  s. A shock wave separates from the He detonation, invades into the CO core, and converges at an off-centered point in the CO core just before  $t = 1.625$  s. Subsequently, a CO detonation occurs at the converging point of the shock wave. Eventually, the primary WD experiences thermonuclear explosion, and the SN ejecta interacts with the companion WD, or to-be surviving WD.

Figure 2 focuses on the time before and after the shock wave converges in the CO core of the primary WD. We can see the shock wave, the density discontinuity in the CO core, is converging from  $t = 1.25$  s to  $t = 1.625$  s, and the CO detonation, density (and temperature) discontinuity, is propagating from  $t = 1.75$  s to  $t = 2$  s. The converging shock wave directly ignites the CO detonation.

We investigate the converging shock wave in detail. Figure 3 shows dynamics of the converging shock wave on a line indicated by the white dashed line in Figure 2. The shock wave fronts pointed by arrows converge at  $y \sim 0$  km. The front propagating in the negative  $y$ -direction is less sharp than in the positive  $y$ -direction, since the former front passes through a denser region, or a region with a higher sound velocity. The shock wave front propagates in the positive (negative)  $y$ -direction at an average velocity of  $\sim 6.7 \cdot 10^3$  km s $^{-1}$  ( $\sim 4.0 \cdot 10^3$  km s $^{-1}$ ) from  $t = 1.25$  s to  $t = 1.625$  s, while the CO core itself moves at a velocity of  $\sim 10^3$  km s $^{-1}$  in the positive  $y$ -direction. Therefore, the velocity of the shock wave front is  $\sim 5.7$  km s $^{-1}$  ( $\sim 5.0$  km s $^{-1}$ ). The corresponding shock wave front has a velocity of  $\sim 4 \cdot 10^3$  km s $^{-1}$  ( $\sim 4 \cdot 10^3$  km s $^{-1}$ ) in (Fink et al. 2010, see Fig. 1). These velocities are roughly consistent. Since the sound velocity at the converging point ( $y \sim 0$  km) is  $\sim 4 \cdot 10^3$  km s $^{-1}$ , the Mach number of the shock wave is  $\sim 1.4$  and  $\sim 1.3$  in the positive and negative  $y$ -directions, respectively.

We can see from Figure 3 that the converging shock wave directly ignites the CO detonation as described above. The shock wave converges just after  $t = 1.625$  s (see the red curve in the top panel of Figure 3). Temperature at the converging point drastically rises between the times at  $t = 1.625$  s and  $t = 1.6406$  s (see the red and black curves in the bottom panel of Figure 3). The temperature at  $t = 1.6406$  s is high enough to ignite carbon materials.

Two high-density, mushroom-shaped, regions are seen in the panels at  $t = 4 - 10$  s. These regions have un-

burned CO materials. Such unburned pockets might be formed due to low mass resolution, although the mass resolution is quite high,  $\sim 2.4 \cdot 10^{-8} M_{\odot}$ . In this paper, we conservatively suppose that these unburned materials could be numerical artifacts. The reason is as follows. We focus on the stage at  $t = 1.8125$  s, when the CO detonation is running in the CO core of the primary WD. These unburned regions can be seen as low-temperature pockets in the bottom panels at  $t = 1.8125$  (or 2 s) in Figure 2. These unburned regions are surrounded by detonated regions with temperatures as high as several  $10^9$  K. From the density and temperature panels at  $t = 1.8125$  s in Figure 2, we find these unburned regions have such high densities as  $\sim 10^8$  g cm $^{-3}$ . Therefore, they are unburned not due to too low densities, but due to blocking the invasion of the CO detonation. However, a CO detonation should never be prevented from propagating into such a high density region.

Hereafter, we do not include these unburned materials in our discussion. For this purpose, we change their chemical compositions to 100 % of  $^{56}\text{Ni}$ . We define these unburned materials as SPH particles satisfying the following three conditions. (1) They originate from the primary WD. These unburned materials come from the primary WD as seen in Figure 2. (2) They are within a distance of  $3 \times 10^5$  km from the coordinate center at  $t = 50$  s. We need this condition in order to avoid erasing unburned materials in the outer SN ejecta apart from the coordinate center by more than  $5 \times 10^5$  km at  $t = 50$  s (see Figure 5). Note that these outer materials are unburned for a physical reason, i.e. due to too low densities. (3) They have the carbon mass fraction more than the critical value of  $X_{\text{C,crit}} = 0.2$  at  $t = 50$  s, since they are unburned. Then the total mass of the unburned materials is  $1.02 \cdot 10^{-2} M_{\odot}$ . We do not choose  $X_{\text{C,crit}} = 0.2$  arbitrarily. In fact, the total mass of the unburned materials is not sensitive to  $X_{\text{C,crit}}$ . If we change  $X_{\text{C,crit}}$  to 0.1 and 0.4, the total mass of the unburned materials increases and decreases by at most  $2 \cdot 10^{-6} M_{\odot}$ , respectively.

The interaction between the SN ejecta and the companion WD forms an ejecta shadow behind the companion WD (see the panels at  $t = 6 - 10$  s), which is similar to an ejecta shadow seen in Papish et al. (2015). The interaction also strips materials of the companion WD, which can be seen as a stream (or streams) denser than its surroundings in the ejecta shadow at  $t = 8$  and 10 s. Hereafter, we call this stream ‘‘companion-origin stream’’. The companion-origin stream flows out after a shock wave, formed by collision between the SN ejecta and companion WD, passes through the companion WD at  $t \sim 8$  s. Note that the shock wave is not



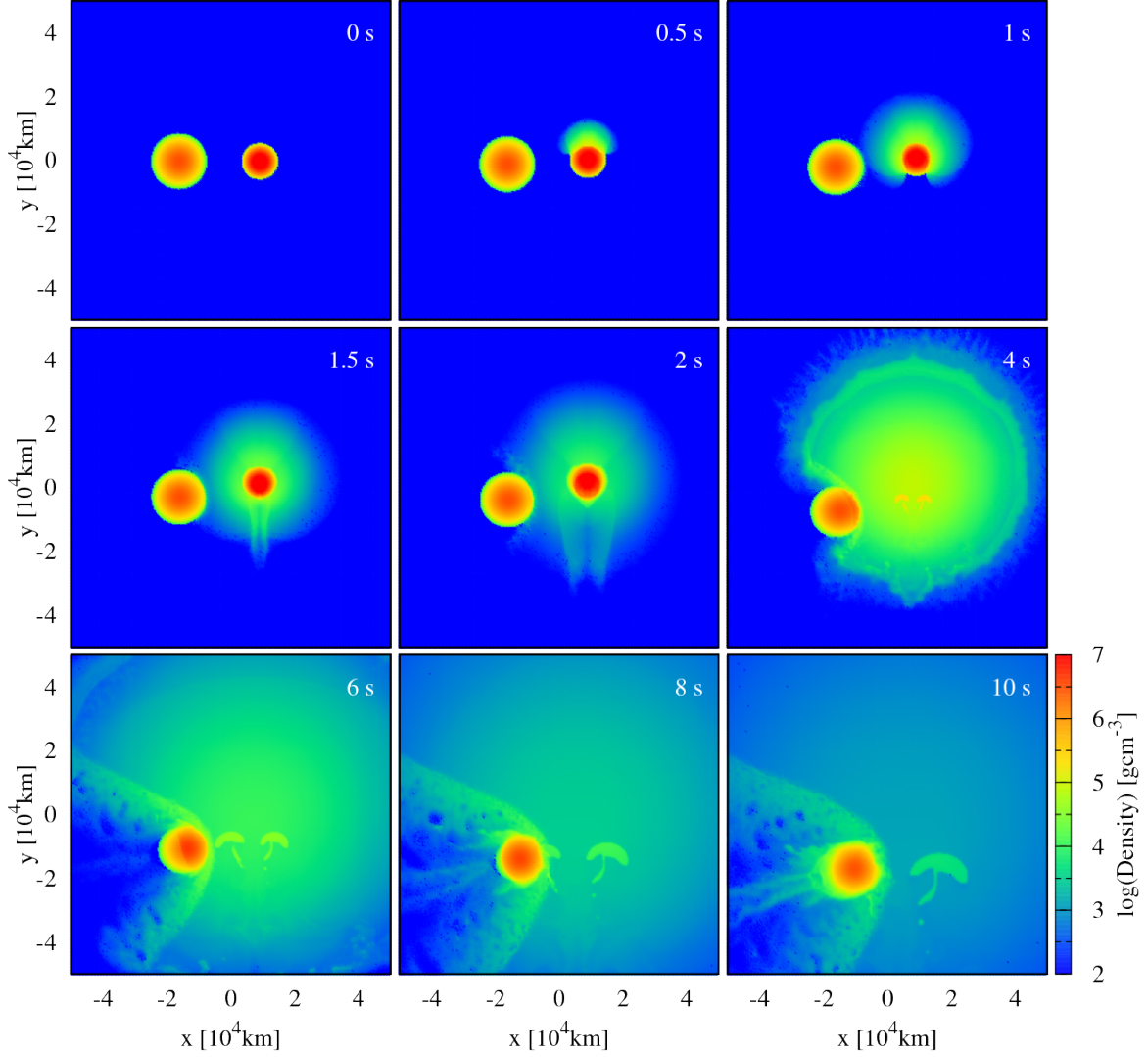


**Figure 1.** Density distribution at  $t = 0, 0.5, 1, 1.5, 2, 4, 8,$  and  $10$  s.

formed by collision between the unburned materials and companion WD. The shock wave can be seen as density discontinuity inside the companion WD in the panel at  $t = 6$  s, and as pressure discontinuity, pointed by white arrows, inside the companion WD in Figure 4.

Figure 5 shows the distribution of density, star ID, and mass fractions of chemical elements at  $t = 50$  s. Note that they are zoomed out 20 times compared to the panels of Figure 1. In the density distribution, we can see the ejecta shadow, circular section-shaped. The surviving (or companion) WD is located at the vertex of the circular section. In the star ID distribution, the surviving WD can be also found at the root of the companion-origin stream. The stream consists of C+O. The solid angles of the ejecta shadow and stream are  $\sim 1.8$  and  $\sim 0.21$  steradians, respectively. The ejecta shadow is much wider than the stream.

Aside from the ejecta shadow and stream, the SN ejecta has a spherically symmetric shape. Chemical elements in the SN ejecta are dominated by Fe-group elements (Cr, Fe, and  $^{56}\text{Ni}$ ), the lighter Si-group elements (Si and S), O, C, the heavier Si-group elements (Ar, Ca, and Ti), and He in order from the inside. The heavier silicon-group elements are the products of the He detonation in the He shell mixed with CO compositions. Such chemical structure is typical of the double detonation model.

As seen in Figure 5, the surviving WD is located far from the coordinate origin by several  $10^4$  km, despite that the binary system is present at the coordinate origin at  $t = 0$  s. This is because the surviving WD flies away free from the gravity of the exploding primary WD. We find the surviving WD has HV of

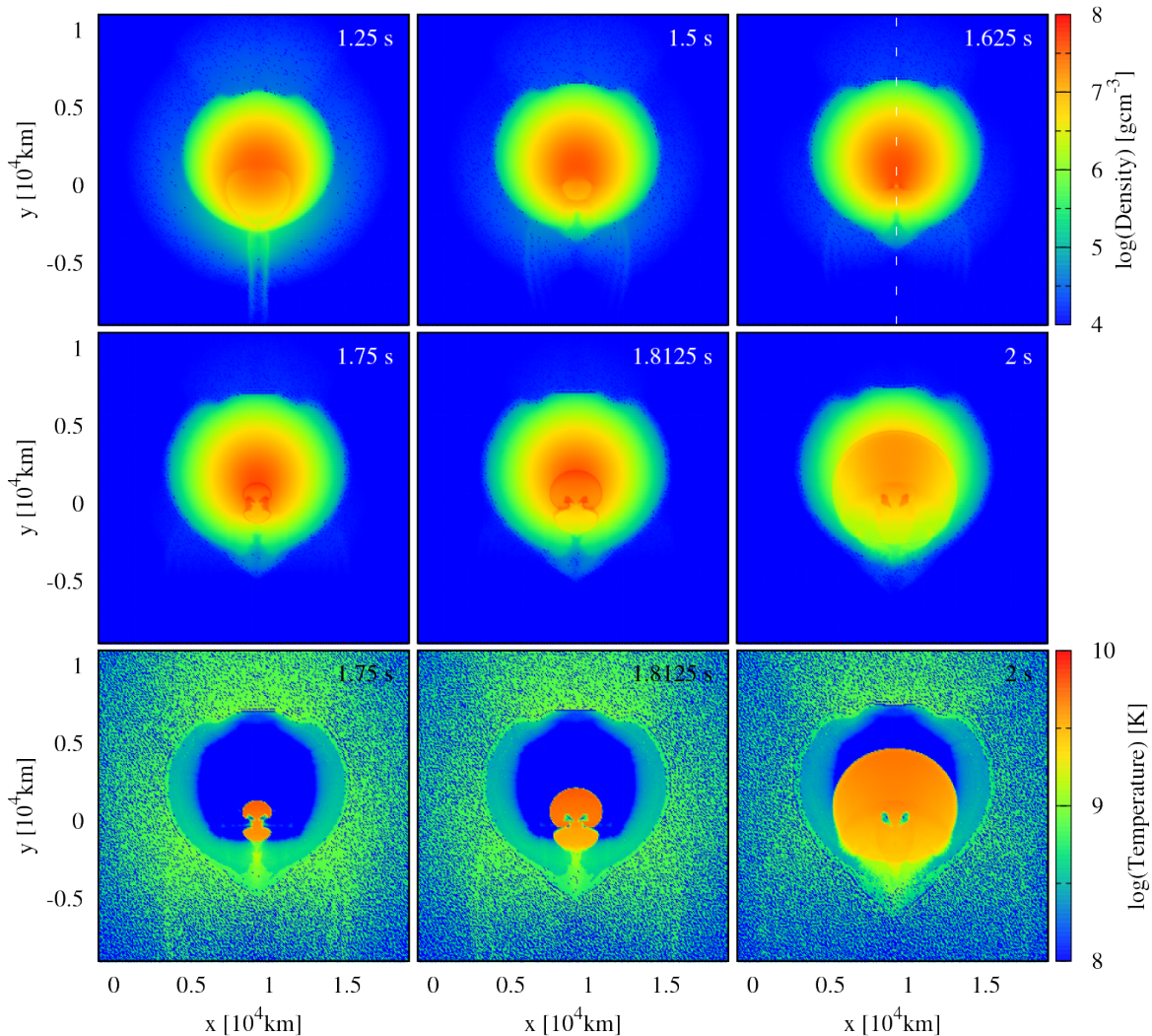


**Figure 2.** Density distribution at  $t = 1.25, 1.5, 1.625, 1.75, 1.8125,$  and  $2$  s, and temperature distribution at  $t = 1.75, 1.8125,$  and  $2$  s in the primary WD. The white dashed line in the panel at  $t = 1.625$  s indicates a column in which a shock wave invading into the CO core converges. The column is focused in Figure 3.

$\sim 1700 \text{ km s}^{-1}$ , consistent with the velocity of the binary motion  $\sim 1800 \text{ km s}^{-1}$ .

### 3.2. Supernova ejecta

#### 3.2.1. $^{56}\text{Ni}$ mass

In Figure 6, we show the mass of chemical elements in the SN ejecta, companion-origin stream, and surviving companion WD. The SN ejecta includes the companion-origin stream. The SN ejecta has  $\sim 0.54M_{\odot}$   $^{56}\text{Ni}$ , most of which are synthesized by the CO detonation in the primary WD. The He detonation yields little  $^{56}\text{Ni}$  ( $\sim 10^{-4}M_{\odot}$ ) because the He shell is small in mass and contains 40 % (in mass fraction) of C+O which are mixed initially. The CO detonation also produces the lighter Si-group elements (Si and S) of  $\sim 0.22M_{\odot}$  through incomplete Si burning. The unburned materi-

als, which do not include the mushroom-shaped materials, are  $\sim 0.07M_{\odot}$  oxygen and  $\sim 0.01M_{\odot}$  carbon. The He detonation synthesizes the heavier Si-group element (Ar, Ca, and Ti) of  $\sim 0.05M_{\odot}$ , especially dominated by Ca.

Figure 7 shows yielded chemical compositions little depend on mass resolutions of SPH simulation as a whole. In detail, the  $^{56}\text{Ni}$  mass is  $\sim 0.54M_{\odot}$  and  $\sim 0.58M_{\odot}$  for the fiducial and higher mass resolutions, respectively, while the Si mass is  $\sim 0.15M_{\odot}$  for both the fiducial and higher mass resolutions. The mushroom-shaped, unburned materials have mass of  $\sim 0.01M_{\odot}$  for both the fiducial and higher mass resolutions. The dependence of the yielded chemical compositions on mass resolution is quite small.

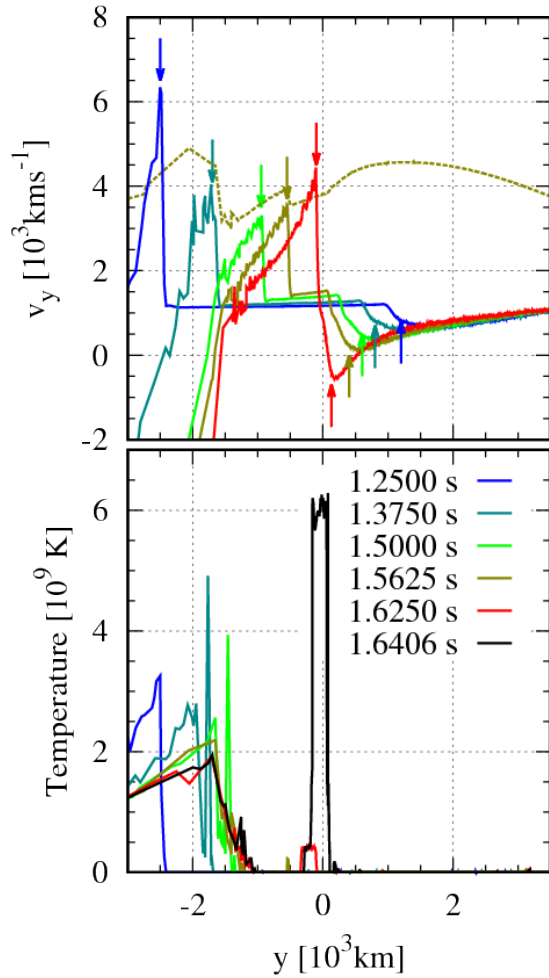


**Figure 3.** Profiles of  $y$ -velocity and temperature in a column in which a shock wave invading into the CO core converges. This column is indicated in the panel at  $t = 1.625$  s of Figure 2. In each panel, we draw each physical quantity at  $t = 1.25, 1.375, 1.5,$  and  $1.625$  s. We also show temperature at  $t = 1.6406$  s. In the  $y$ -velocity panel, we point to shock wave fronts by arrows, and indicate the sound velocity profile at  $t = 1.5625$  s by a dashed curve as reference.

In order to evaluate an error of chemical compositions of SN ejecta, we adopt Jackknife resampling. We divide all the SPH particles into 16 subgroups by sampling one SPH particle per 16 SPH particles from SN ejecta. For each subgroups, we count masses of chemical elements and multiply these masses by 16. We can see from Figure 7 that chemical compositions are the same among the original data and subgroups. Therefore, sampling bias is almost zero.

We compare our nucleosynthesis yields with those in models 2 of Fink et al. (2010), which has the CO core of  $0.920M_{\odot}$  and the He shell of  $0.084M_{\odot}$ , being similar to our primary WD. We focus only on the products of CO detonation, since their He shell consists of pure He. Our

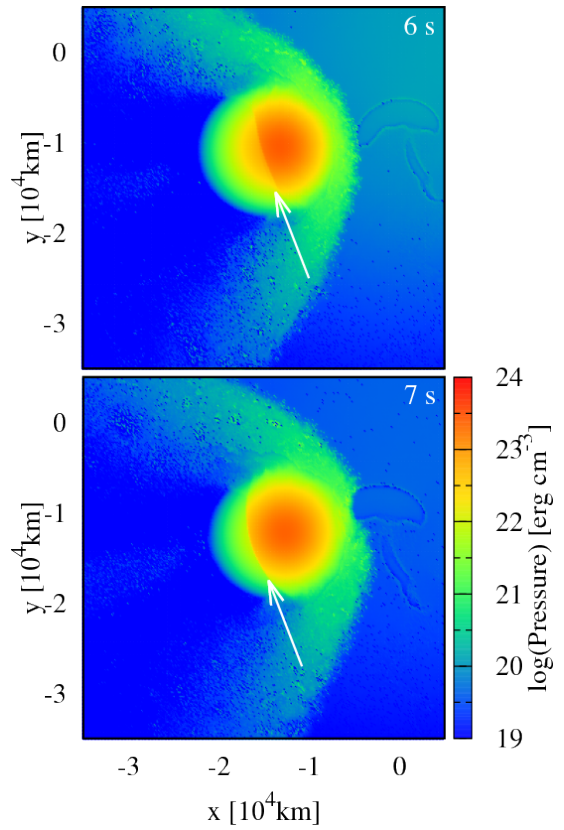


**Figure 4.** Pressure distribution at  $t = 6$  and  $7$  s. White arrows point to the pressure discontinuity.

$^{56}\text{Ni}$  mass ( $\sim 0.54M_{\odot}$ ) is larger than theirs ( $0.36M_{\odot}$ ), while our Si-group mass ( $0.22M_{\odot}$ ) is smaller than theirs ( $0.44M_{\odot}$ ). We also compare our products of CO detonation with those of Woosley & Kasen (2011). In their models with the primary WD of  $\sim 1M_{\odot}$ ,  $^{56}\text{Ni}$  masses are  $0.5M_{\odot} - 0.8M_{\odot}$ . Our nucleosynthesis yields are roughly consistent with those in previous studies. However, further detailed nucleosynthesis studies are necessary to reach a better agreement.

### 3.2.2. Nucleosynthesis yields in the velocity space

The total mass of the companion-origin stream is  $\sim 3 \cdot 10^{-3}M_{\odot}$ . It consists of mostly 50 % carbon and 50 % oxygen in mass, being almost the same as the original compositions, but includes a small amount of Ne, Mg, and Si,  $\sim 10^{-7}M_{\odot}$  for each. They are synthesized by shock heating when the SN ejecta collides with the companion WD.

Figure 8 shows the chemical elements in mass as a function of the radial velocity. We average the mass fractions over all the angle, and find that the abundance structure is similar to the typical double detonation model. The first high-velocity components ( $\gtrsim 2 -$



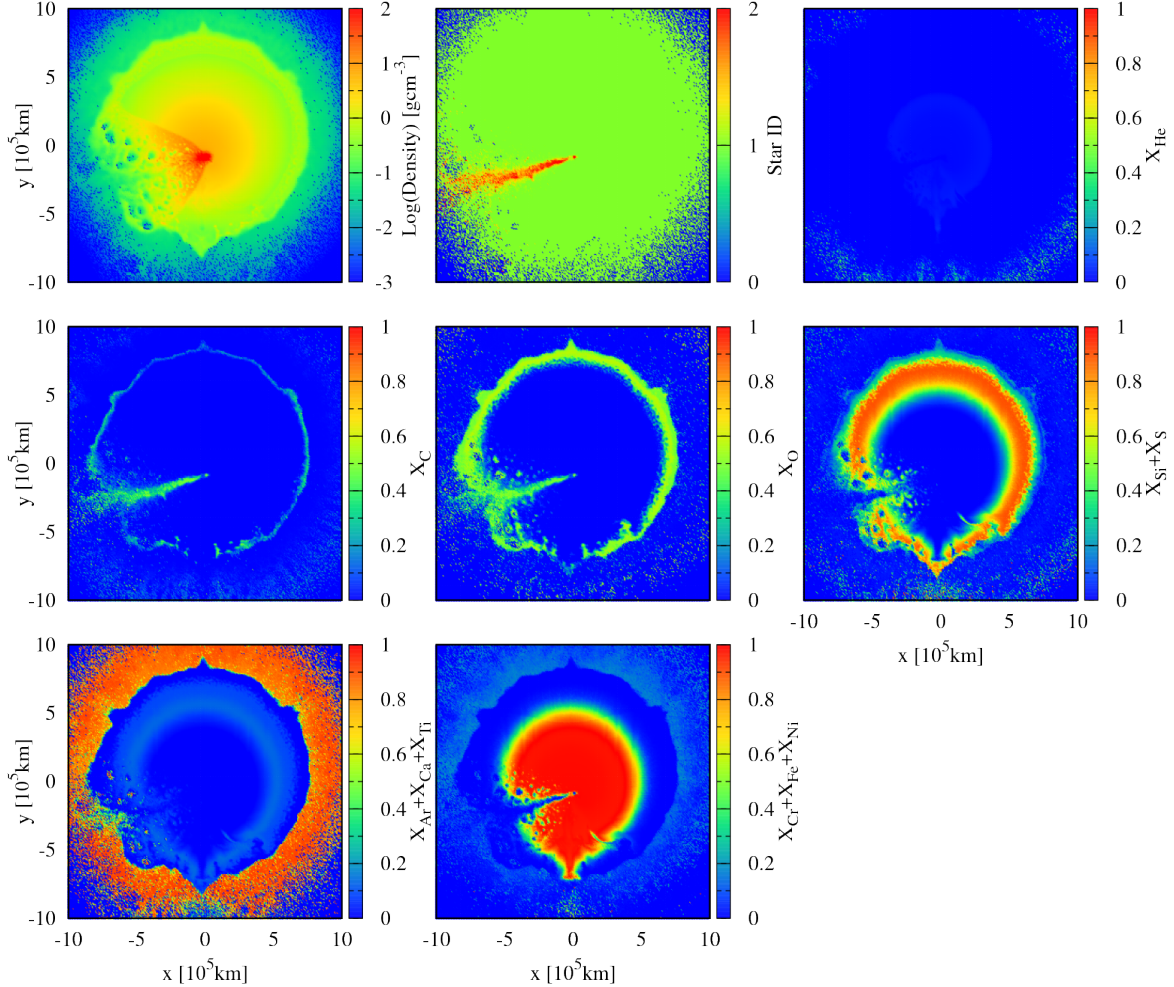


**Figure 5.** Distribution of density, star ID, and mass fractions of chemical elements at  $t = 50$  s. Note that, if there is no material, the star IDs “0” are assigned. We change the mushroom-shaped, unburned materials to 100 %  $^{56}\text{Ni}$  materials. This is also true for Figures 6, 7, 8, 9, and 10.

$3 \cdot 10^4 \text{ km s}^{-1}$ ) consist of Ca and Ti, synthesized by the He detonation. The second high-velocity components ( $\sim 1.5 - 2 \cdot 10^4 \text{ km s}^{-1}$ ) are composed of C+O, unburned materials located at the outer region in the CO core of the primary WD. Behind the unburned materials, the third high-velocity components ( $\sim 1 - 1.5 \cdot 10^4 \text{ km s}^{-1}$ ) includes Si and S, products of incomplete silicon burning. Low-velocity components ( $< 10^4 \text{ km s}^{-1}$ ) are composed of  $^{56}\text{Ni}$ . The low-velocity components contain a slight amount of C+O at the velocity of  $\sim 3 \cdot 10^3 \text{ km s}^{-1}$ , described below in detail.

The low-velocity C+O come from the companion-origin stream. The features show up from the view into which the stream comes,  $(\theta, \phi) = (90^\circ, 210^\circ)$  and  $(90^\circ, 240^\circ)$ . Interestingly, the chemical structure from these views is the same as the averaging structure at the velocity of  $> 10^4 \text{ km s}^{-1}$ . Therefore, C+O have bimodality in the velocity distribution. One compo-

nent has a higher velocity than Si and S ( $\sim 1.5 - 2 \cdot 10^4 \text{ km s}^{-1}$ ), and the other has a lower velocity ( $\sim 3 \cdot 10^3 \text{ km s}^{-1}$ ). Moreover, the low-velocity C+O have a velocity dependent on the viewing angle,  $\gtrsim 3 \cdot 10^3 \text{ km s}^{-1}$  from the view of  $(\theta, \phi) = (90^\circ, 210^\circ)$ , and  $\lesssim 3 \cdot 10^3 \text{ km s}^{-1}$  from the view of  $(\theta, \phi) = (90^\circ, 240^\circ)$ .

We emphasize that the low-velocity C+O originate from the companion-origin stream, not from the unburned materials of the primary WD. As seen in the star-ID panel of Figure 5, the companion-origin stream comes into sight from the viewing angles  $(\theta, \phi) = (90^\circ, 210^\circ)$  and  $(90^\circ, 240^\circ)$ . Moreover, we change the mushroomed-shaped, unburned materials to materials 100 %  $^{56}\text{Ni}$  as described above.

The distribution of C+O in our SN ejecta is different from the delayed detonation model (Seitenzahl et al. 2013; Leung & Nomoto 2018), although both models have low-velocity C+O. In the delayed detonation



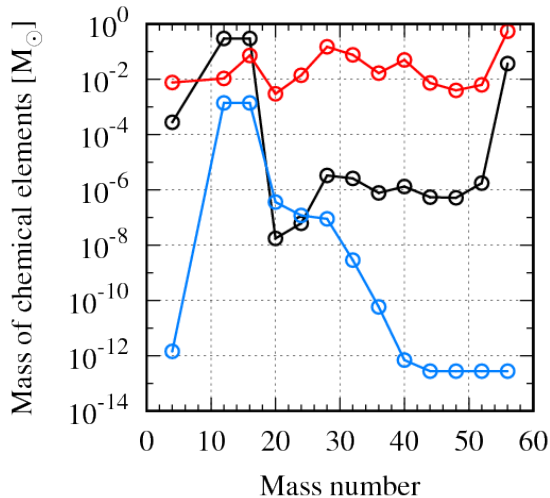


**Figure 6.** Masses of chemical elements in the SN ejecta (red), companion-origin stream (blue) and surviving WD (black) at  $t = 50$  s. The SN ejecta includes the companion-origin stream. Materials of the SN ejecta and surviving WD are gravitationally unbound and bound to the surviving WD, respectively.

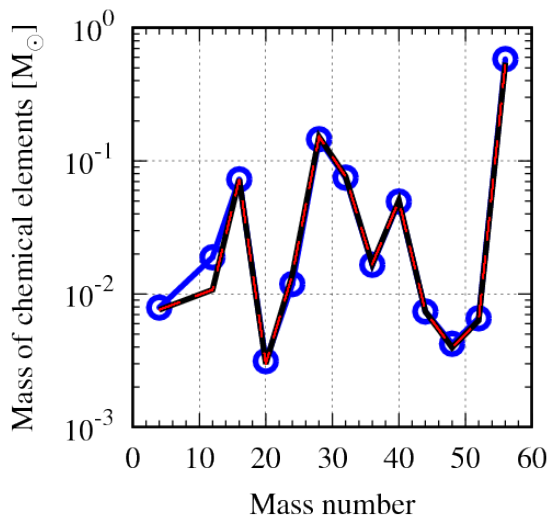


**Figure 7.** Mass of chemical elements for the original data (black), and 16 subgroups of SN ejecta (red) from the fiducial mass-resolution simulation, and data from the higher mass-resolution simulation (blue). The black and red curves overlay each other, since the chemical compositions are the same.

model, C+O are extended from the high-velocity to low-velocity components. On the other hand, C+O in our SN ejecta have two peaks in the velocity space.

No low-velocity C+O can be seen from other views  $\theta = 0^\circ$  and  $180^\circ$ , and  $(\theta, \phi) = (90^\circ, 45^\circ)$ ,  $(90^\circ, 135^\circ)$ , and  $(90^\circ, 315^\circ)$ , since the stream does not come into these sights. The velocity distributions of chemical elements from these viewing angles are the same as those

in the double detonation model, such that materials are dominated by the He-detonation products (Ca and Ti), unburned materials (CO compositions), incomplete silicon burning products (Si and S), and  $^{56}\text{Ni}$  in the descending order of the velocity.

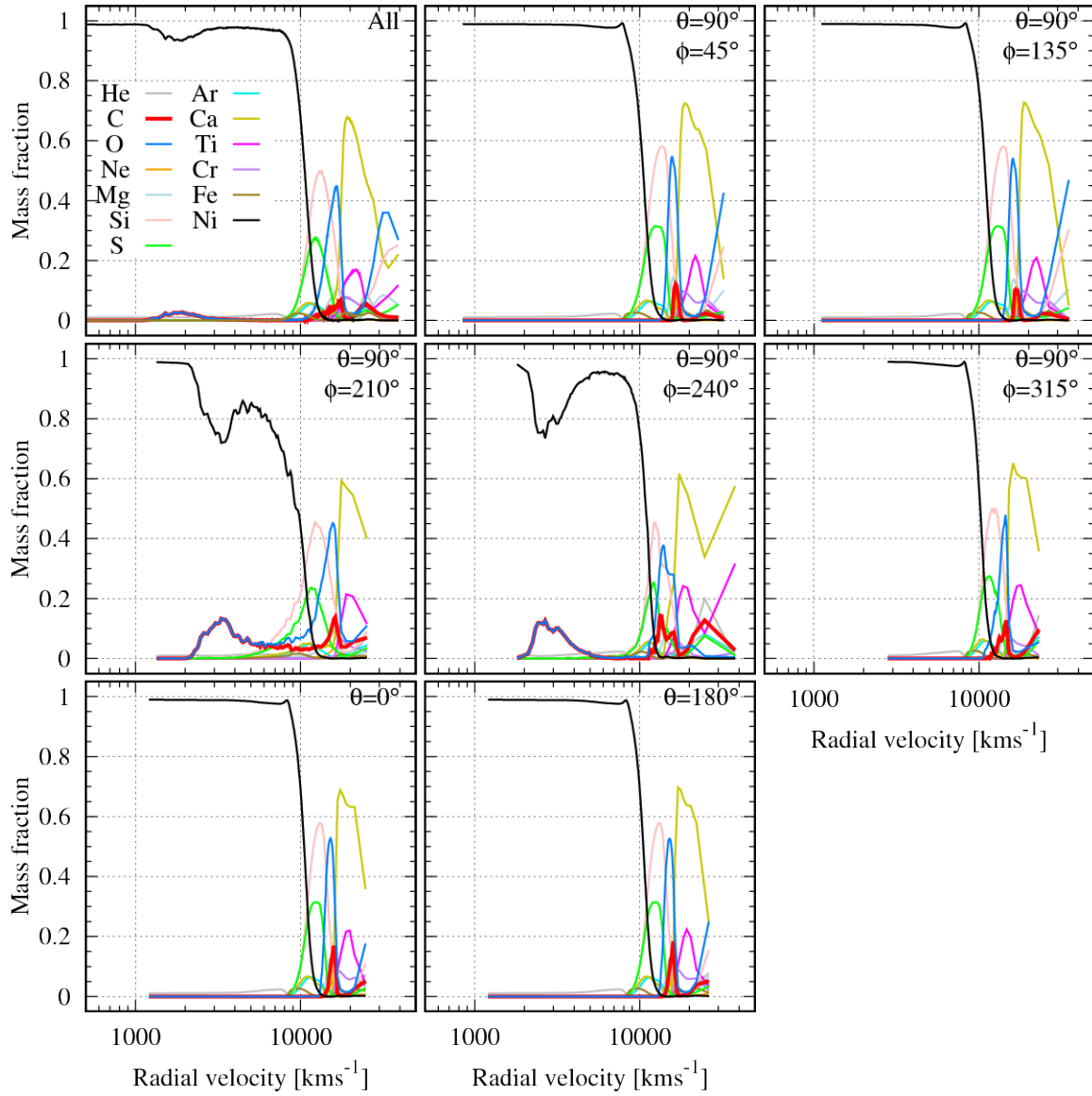
The surviving WD moves at a speed of  $1700 \text{ km s}^{-1}$  in the bottom-right direction (closely to  $(\theta, \phi) = (90^\circ, 315^\circ)$ ) in Figure 5, not only at  $t = 50$  s but also at the explosion time of the primary WD. Hence, the primary WD also propagates at a speed of  $\sim 1100 \text{ km s}^{-1}$  in the opposite direction (closely to  $(\theta, \phi) = (90^\circ, 135^\circ)$ ) at the explosion time. Therefore, the SN ejecta should be shifted in the propagating direction of the exploding primary WD.

Figure 9 shows the velocity distribution of O, Si, and  $^{56}\text{Ni}$  observed from various viewing angles. All chemical elements have higher velocities for the viewing angles closer to the direction of the bulk velocity of the SN ejecta. The velocity difference is  $\sim 1 - 2 \cdot 10^3 \text{ km s}^{-1}$  between  $(\theta, \phi) = (90^\circ, 135^\circ)$  and  $(\theta, \phi) = (90^\circ, 315^\circ)$ . The velocity of these elements observed from the other viewing angles is intermediate between the velocity observed from the two viewing angles. This is consistent with the velocity of the binary motion of the exploding primary WD,  $1100 \text{ km s}^{-1}$ .

The velocity difference does not come from the asymmetric explosion of the double detonation model. In the asymmetric explosion, when the velocity of O and Si from a viewing angle is larger than from another viewing angle, the velocity of  $^{56}\text{Ni}$  from the former is smaller than from the latter (see Fig. 6 in Fink et al. 2010). Note that the bulk motion of the exploding primary WD (or SN ejecta) systematically increases all the velocity of O, Si, and  $^{56}\text{Ni}$  observed from the viewing angle in the propagating direction.

### 3.3. Surviving white dwarf

The surviving WD has the total mass of  $\sim 0.6M_\odot$ , roughly equal to the initial mass. However, it captures a small amount of materials originally from the exploding primary WD. The total mass of the captured materials is  $\sim 0.03M_\odot$ , dominated by  $^{56}\text{Ni}$  of  $\sim 0.03M_\odot$  (or  $^{56}\text{Ni}$  of  $\sim 0.02M_\odot$  unless we change the mushroomed-shaped, unburned materials to materials of 100 %  $^{56}\text{Ni}$ ). The captured materials contain slight amount of helium ( $\sim 3 \cdot 10^{-4}M_\odot$ ). The captured materials consist of  $^{56}\text{Ni}$  and He in the following reason. They are captured due to their low velocity. Hence, they are located at the center of the explosion, i.e. in a high-density region. In general, when CO detonation passes a high-density region, it mostly synthesizes  $^{56}\text{Ni}$  owing to the rapid nuclear reactions, and leaves a small amount of He as



**Figure 8.** Chemical elements in mass fraction as a function of radial velocity.

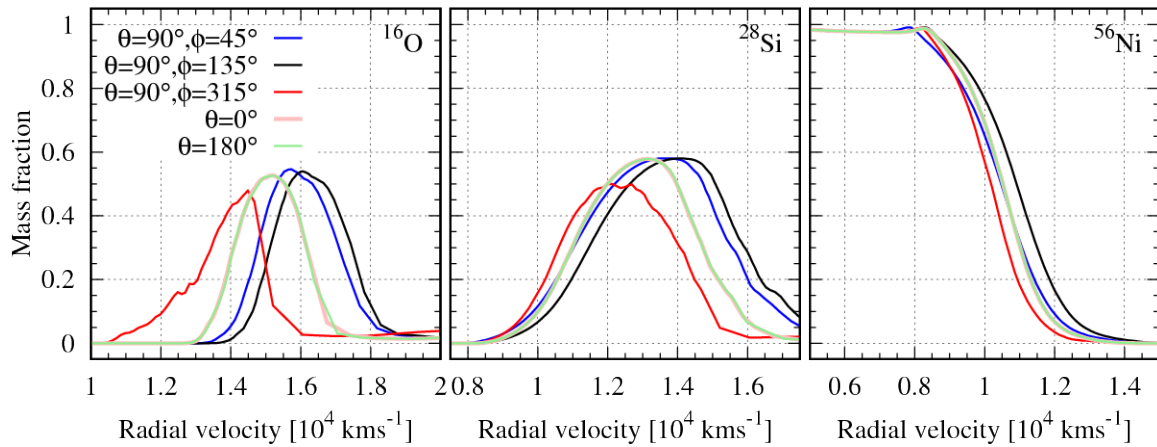


**Figure 9.** Mass fractions of oxygen, silicon, and nickel as a function of the radial velocity.

residuals of He produced by photo-dissociation. Shen &

Schwab (2017) have estimated that a  $0.6M_{\odot}$  WD captures  $0.03M_{\odot}$   $^{56}\text{Ni}$ , which is consistent with our results.

We investigate 1D profiles of the surviving WD at  $t = 50$  s shown in Figure 10, where we count only gravitationally bound materials to the surviving WD. We find its internal structure (at  $r \lesssim 7 \cdot 10^3$  km) is virtually undamaged, comparing its density, temperature, and entropy profiles at  $t = 0$  and 50 s. Moreover, the surviving WD keeps its C+O.

On the other hand, its external structure is changed by the interaction with the SN ejecta. The surviving WD captures a part of the SN ejecta, and gets an envelope consisting of  $^{56}\text{Ni}$ , C, O, and He in descending order in mass. These  $^{56}\text{Ni}$  and He result from nucleosynthesis in the primary WD, while C and O come from the surviving WD. Note again that we change the mushroom-shaped, unburned materials to materials of 100 %  $^{56}\text{Ni}$ . The C and O originally from the surviving WD are modestly stripped from the surviving WD by the SN ejecta. The envelope has high temperature ( $\sim 2.5 \cdot 10^8$  K) and entropy ( $\sim 4.5 \cdot 10^8$  erg  $\text{g}^{-1}$   $\text{K}^{-1}$ ) due to nuclear reactions in the primary WD, and due to the shock heating arising from the collision between the SN ejecta and surviving WD. The entropy of the captured materials is slightly higher than estimated by Shen & Schwab (2017),  $1 - 3 \cdot 10^8$  erg  $\text{g}^{-1}$   $\text{K}^{-1}$ . Hence, the captured materials are slightly less bound than their estimate.

## 4. DISCUSSION

### 4.1. Exploding primary white dwarf

First, we discuss SN Ia counterparts to the  $\text{D}^6$  model, based on the results shown in section 3. Here, we ignore products yielded by the He detonation, which are the heavy Si-group elements (Ar, Ca, and Ti) with such high velocities,  $\gtrsim 2 \cdot 10^4$  km  $\text{s}^{-1}$ . This reason is as follows. We set the He shell of the primary WD to be so thick ( $\sim 0.05M_\odot$ ) that the He and CO detonation easily occurs in our simulation. However, the  $\text{D}^6$  model would succeed when the He shell is  $\lesssim 0.01M_\odot$  (Guillochon et al. 2010; Pakmor et al. 2013), and would indicate smaller signal of these products than our simulation results.

The most prominent feature in our SN ejecta is the companion-origin stream (see Figure 5). Owing to the presence of the stream, the abundance of unburned materials has two peaks in velocity space from specific viewing angles, as seen in Figure 8. The lower velocity component of the unburned materials (a few  $10^3$  km  $\text{s}^{-1}$ ) can be observed as oxygen emission lines in nebular-phase spectra. Such oxygen emission lines have been observed in SN 2002cx-likes (Jha et al. 2006; Phillips et al. 2007), and a part of SN 2002es-like SN 2010lp (Taubenberger et al. 2013; Kromer et al. 2013) and iPTF14atg (Kromer et al. 2016). In SN 2002cx-likes, possibly explained by

pure-deflagration explosion (Kozma et al. 2005) (but see Wang et al. 2013),  $^{56}\text{Ni}$  prevails from the inner to outer ejecta, while our SN ejecta confines  $^{56}\text{Ni}$  to the inner parts with  $\lesssim 10^4$  km  $\text{s}^{-1}$ . Hence, we rule out SN 2002cx-likes as  $\text{D}^6$  explosion candidates.

SN 2010lp and iPTF14atg could be promising counterparts to  $\text{D}^6$  model, since their light curves and spectral evolutions are consistent with the explosion of sub-Chandrasekhar mass WDs (Kromer et al. 2013, 2016, respectively). Although iPTF14atg have ultraviolet (UV) pulse due to collision of the SN ejecta with the non-degenerate companion (Cao et al. 2015), the UV pulse could be explained by surface radio activity of  $^{56}\text{Ni}$  produced by the He detonation (Kromer et al. 2016). However, our SN ejecta may be inconsistent with SN 2010lp. SN 2010lp has both blue- and red-shifted oxygen emissions in its nebular spectra. On the other hand, our SN ejecta would have either of blue- or red-shifted oxygen emissions, since the companion-origin ejecta stream propagates in one direction from the explosion center. Note that it may be difficult to identify these oxygen emissions, since the companion-origin stream has small mass ( $\sim 3 \cdot 10^{-3}M_\odot$ ). We need to study nebular-phase spectra of the  $\text{D}^6$  model by performing radiative transfer calculations (e.g. Maeda et al. 2010; Botyánszki & Kasen 2017).

We should note that these oxygen feature may not be observed in the following reason. The companion WD should have a He shell in reality, although it does not have in our setup. If the He shell has more than  $\sim 3 \cdot 10^{-3}M_\odot$ , the SN ejecta may strip only the He shell, not the CO core. Therefore, the companion-origin stream can consist of He materials. Nevertheless, the companion-origin stream can contain CO because of mixing of CO into the overlying He shell during common envelope phase and merging process as mentioned for the He shell of a primary WD. Even though the He shell has more than  $\sim 3 \cdot 10^{-3}M_\odot$ , C+O is likely mixed in the companion-origin stream. Moreover, a companion WD with larger mass has smaller He shell mass. Eventually, the presence and absence of oxygen features depends on detail binary parameters of progenitor systems. In future, we will investigate compositions of companion-origin streams in the cases of companion WDs with different total and He shell masses.

Another feature is the velocity shift of SN ejecta due to the binary motion of the primary WD,  $\sim 10^3$  km  $\text{s}^{-1}$ . Maeda et al. (2011) have shown iron and nickel emission lines can be tracers of such a velocity shift. Dong et al. (2018) have compiled cobalt emissions in nebular spectra of various SNe Ia, and have found the cobalt emissions are both blue- and red-shifted in SNe Ia

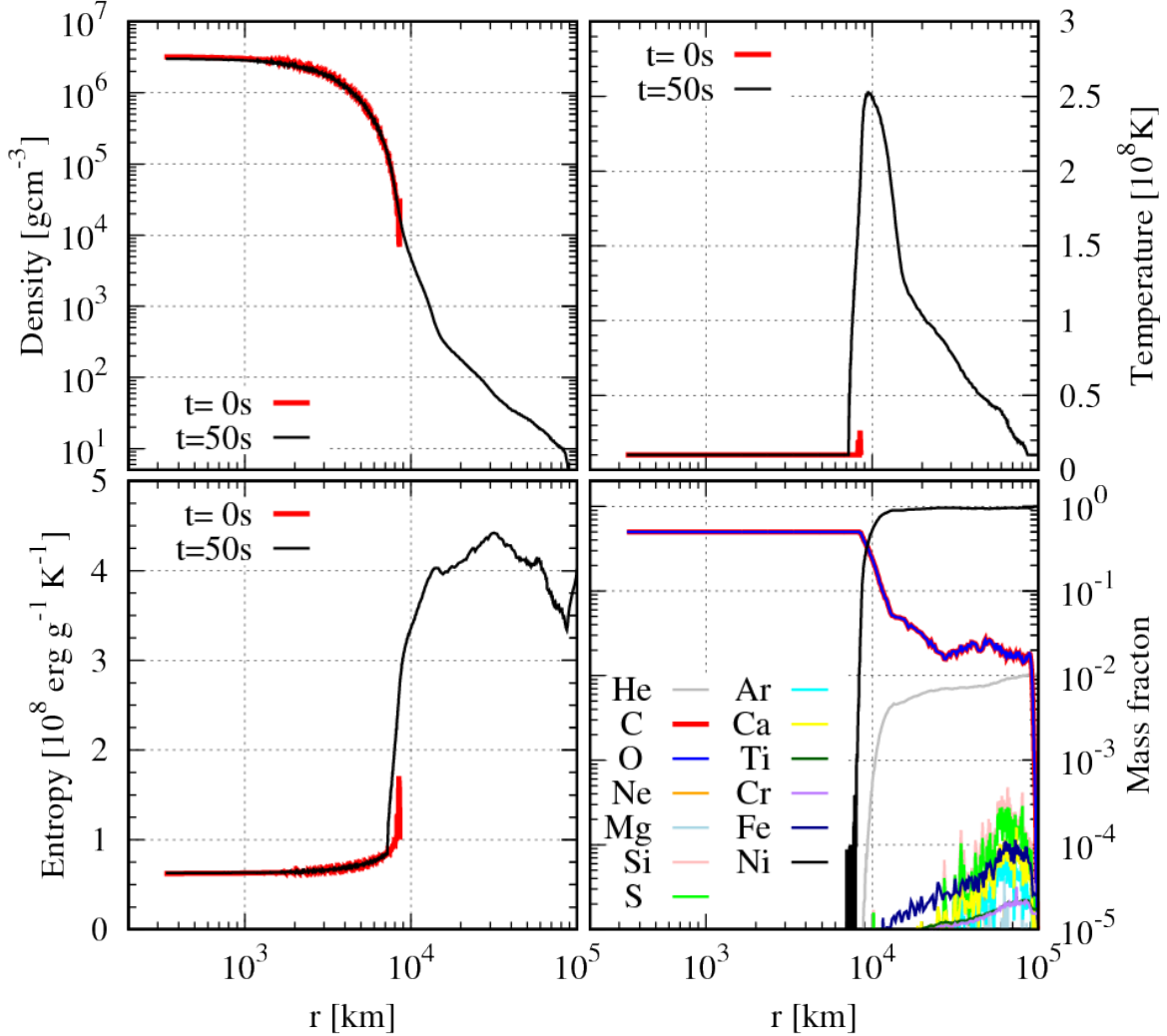


**Figure 10.** 1D profiles of density, temperature, and entropy of the companion WD at  $t = 0$  s (red) and  $t = 50$  s (black), and of chemical elements of the companion WD at  $t = 50$  s.

with  $-19 < M_B < -18$  (SN 2007on, SN 2003hv, and SN 2003gs), and either blue- or red-shifted in those with  $M_B > -18$  (SN 2016brx, SN 2005ke, SN 1999by, and SN 1991bg). Although they have attributed these blue- and red-shifted features to the collisional DD model (Benz et al. 1989; Lorén-Aguilar et al. 2010; Raskin et al. 2009, 2010; Rosswog et al. 2009; Hawley et al. 2012; Dong et al. 2015), SNe Ia with either of blue- or red-shifted Fe-group emissions can be also explained by the  $D^6$  model.

#### 4.2. Surviving white dwarf companion

Hereafter, we describe issues related to the surviving WD. Shen & Schwab (2017) have discussed post-supernova winds blown by radioactive  $^{56}\text{Ni}$  on the surfaces of surviving WDs. We can compare our results with their surviving CO WD model with  $0.6M_\odot$ . They have modeled the surface of the surviving CO WD, such

that the mass of radioactive  $^{56}\text{Ni}$  is  $0.0003 - 0.03M_\odot$ , and the entropy of its surface is  $1 - 3 \cdot 10^8 \text{ erg g}^{-1} \text{ K}^{-1}$ . As we obtain the  $^{56}\text{Ni}$  mass and entropy on the surface of the surviving WD to be  $\sim 0.03M_\odot$ , and  $4.5 \cdot 10^8 \text{ erg g}^{-1} \text{ K}^{-1}$ , our simulation results are consistent with their modeling, although materials on the surface in our results are slightly less bound than those in their models. Thus, SN 2011fe could not be explained by the  $D^6$  model, which is the same conclusion as theirs. This is because SN 2011fe would be more luminous than observed if it contained a surviving WD.

We discuss the surface abundance of the surviving WD. First, we consider the surface pollution by interstellar medium (ISM) and interstellar objects (ISOs). The surviving WD could accrete ISM through the Bondi-Hoyle-Lyttleton accretion. The accreting mass is esti-



mated as

$$\begin{aligned}
M_{\text{acc}} &\sim \dot{M}_{\text{acc,BHL}} T_{\text{disk}} \\
&\sim \frac{\pi \rho_{\text{ism}} G^2 M_{\text{wd}}^2 h_{\text{disk}}}{c_{\text{s,ism}}^4 v_{\text{wd}}} \\
&\sim 1.0 \cdot 10^{20} \left( \frac{n_{\text{ism}}}{1 \text{cm}^3} \right) \left( \frac{c_{\text{s,ism}}}{20 \text{km s}^{-1}} \right)^{-4} \left( \frac{h_{\text{disk}}}{200 \text{pc}} \right) \\
&\times \left( \frac{M_{\text{wd}}}{0.6 M_{\odot}} \right) \left( \frac{v_{\text{wd}}}{2000 \text{km s}^{-1}} \right)^{-1} \text{ [g]}, \quad (1)
\end{aligned}$$

where  $\dot{M}_{\text{acc,BHL}}$  is the mass accretion rate through Bondi-Hoyle-Lyttleton accretion,  $T_{\text{disk}}$  is time the surviving WD spending in the Galactic disk,  $\rho_{\text{ism}}$ ,  $n_{\text{ism}}$ , and  $c_{\text{s,ism}}$  are, respectively, ISM mass density, number density, and sound speed,  $h_{\text{disk}}$  is the scale height of the Galactic disk, and  $M_{\text{wd}}$  and  $v_{\text{wd}}$  are the mass and velocity of the surviving WD. Note that this estimate constrains on the upper limit of the accreting mass (Krumholz et al. 2006). Moreover, we estimate a collision rate of the surviving WD with ISOs like 11/‘Oumuamua (Meech et al. 2017). The estimate method is the same as in Tanikawa et al. (2018). Then, the surviving WD collides with ISOs at most once, and accrete the ISO mass of  $\sim 10^{13}$  g at most. Eventually, the surviving WD accretes ISM and ISO mass much less than materials captured from the SN ejecta by several orders of magnitude. Hence, ISM and ISOs cannot pollute the surface of the surviving WD.

As shown in section 3.3, the surviving WD captures  $^{56}\text{Ni}$  of  $\sim 0.03 M_{\odot}$ , and He of  $\sim 3 \cdot 10^{-4} M_{\odot}$ . The  $^{56}\text{Ni}$  of  $\sim 0.03 M_{\odot}$  actually includes the mushroom-shaped, unburned materials of  $\sim 0.01 M_{\odot}$ . Even if the unburned materials are not numerical artifacts, they cannot be regarded as anomaly, since the surviving WD also has similar unburned materials. The  $^{56}\text{Ni}$  will undergo radioactive decay. The  $^{56}\text{Ni}$  decay products could be identified as anomalous abundances. However, the decay products do not necessarily stay on the surface of the surviving WD, since they will receive sedimentation (Paquette et al. 1986; Dupuis et al. 1992). Note that they can keep their position due to radiative levitation (Chayer et al. 1995a,b). It must be necessary to perform sophisticated numerical calculation to follow the time evolution of the surviving WD if we know whether the decay products stay on the surface of the surviving WD. Here, we do not perform such calculations.

The surviving WD certainly has He on its surface, since He does not experience sedimentation. However, it is difficult to assess whether a HV WD is a surviving WD against the  $D^6$  explosion on the basis of the detection of He in the following two reasons. First, the detection of He on a HV WD cannot be the smoking-gun

evidence that the HV WD is a surviving WD against the  $D^6$  explosion. Since WDs generally have He on its surface, a HV WD gets its HV through mechanism other than the  $D^6$  explosion. Second, the non-detection of He on a HV WD’s surface does not always deny the HV WD is a  $D^6$  candidate. He on a HV WD’s surface can be seen only when the HV WD has high temperature on its surface. In fact, Shen et al. (2018) did not find He on the surface of their HV WDs (WD1) for this reason. In summary, we can say a HV WD is not a surviving WD against the  $D^6$  explosion only if He is not detected despite of high temperature on the HV WD’s surface. We reemphasize WD1 in Shen et al. (2018) can be a surviving WD against the  $D^6$  explosion despite of the non-detection of He, since WD1’s surface has low temperature.

Since LP 40–365 (or GD 492) has high abundance of Mn and other iron group elements, it is thought to be a WD candidate surviving against the Type Ia explosion (Vennes et al. 2017; Raddi et al. 2018b,a). Such abundance pattern could not be reconciled with the  $D^6$  explosion, since the  $D^6$  explosion involves sub-Chandrasekhar mass WD.

## 5. SUMMARY

In order to study features of SN ejecta and surviving WD in the  $D^6$  model, we perform SPH simulation of a binary star system with  $1.0 M_{\odot}$  and  $0.6 M_{\odot}$  CO WDs, where the primary WD has a He shell with  $0.05 M_{\odot}$  mixed with C+O. The primary WD undergoes thermonuclear explosion following the He detonation on the shell and the CO detonation in the core. The SN ejecta collides with the companion WD, and the interaction of the SN ejecta with the companion WD form the ejecta shadow and companion-origin stream. Papish et al. (2015) have also found out such ejecta shadows in their simulations for their  $D^6$  models. The companion WD survives the explosion of the primary WD, and flies away at velocity of  $\sim 1700 \text{ km s}^{-1}$  as the surviving WD.

The SN ejecta has typical features of the double detonation explosion on average. However, there are two different features from the double detonation explosion. (1) First, the SN ejecta strips materials of the companion WD, and contains the companion-origin ejecta consisting of C+O. The companion-origin ejecta can make oxygen emission lines in nebular-phase spectra. Therefore, SN Ia counterparts to the  $D^6$  model can be a part of SN 2002es-like, such as SN 2010lp and iPTF14atg which have oxygen emission lines in their nebular-phase spectra. Note that the compositions of the companion-origin ejecta may depend on the He shell mass of the companion WD. In future, we will investigate this de-

pendence. (2) Second, the SN ejecta has velocity shift of  $\sim 1000 \text{ km s}^{-1}$  due to the binary motion of the exploding primary WD. This velocity shift can result in blue- or red-shifted Fe-group emission lines in nebular-phase spectra seen in sub-luminous SNe Ia, such as SN 2016brx, SN 2005ke, SN 1999by, and SN 1991bg.

The surviving WD certainly has He on its surface. The He originates from residuals of He produced by photodissociation at the center of the primary WD. However, since WDs generally have He on their surfaces, the presence of He could not be the smoking-gun evidence of surviving WDs against the  $D^6$  explosion. The surviving WD also has  $^{56}\text{Ni}$  decay products on its surface just after it survives the explosion of the primary WD. However, the decay products would experience sedimentation and radiative levitation. In order to determine the surface abundance of the surviving WD, we should follow the long-term evolution of the surviving WD.

Finally, we summarize observational features of SNe Ia under the  $D^6$  explosion. At an early time, its light curve may show a UV pulse due to radioactive nuclei yielded by the He detonation. At the maximum-light time, its spectra indicate Si absorption lines similarly to ordinary SNe Ia. At late times, in the nebular-phase, oxygen emission lines can be observed, where the oxygen originates from the companion-origin stream stripped by the SN ejecta. From specific viewing angles, blue- or red-

shifted Fe-group emission lines can be also seen due to the binary motion of the exploding primary WD.

Numerical computations were carried out on Oakforest-PACS at Joint Center for Advanced High Performance Computing, and on Cray XC50 at Center for Computational Astrophysics, National Astronomical Observatory of Japan. The software used in this work was in part developed by the DOE NNSA-ASC OASCR Flash Center at the University of Chicago. This research has been supported by World Premier International Research Center Initiative (WPI Initiative), MEXT, Japan, by the Endowed Research Unit (Dark side of the Universe) by Hamamatsu Photonics K.K., by MEXT program for the Development and Improvement for the Next Generation Ultra High-Speed Computer System under its Subsidies for Operating the Specific Advanced Large Research Facilities, by “Joint Usage/Research Center for Interdisciplinary Large-scale Information Infrastructures” and “High Performance Computing Infrastructure” in Japan (Project ID: jh180021-NAJ), and by Grants-in-Aid for Scientific Research (16K17656, 17K05382, 17H06360) from the Japan Society for the Promotion of Science.

*Software:* Modules of Helmholtz EoS and Aprox13 in FLASH (Fryxell et al. 2000, 2010)

## REFERENCES

- Benvenuto, O. G., Panei, J. A., Nomoto, K., Kitamura, H., & Hachisu, I. 2015, *ApJL*, 809, L6
- Benz, W., Hills, J. G., & Thielemann, F.-K. 1989, *ApJ*, 342, 986
- Botyánszki, J., & Kasen, D. 2017, *ApJ*, 845, 176
- Cao, Y., Kulkarni, S. R., Howell, D. A., et al. 2015, *Nature*, 521, 328
- Chayer, P., Fontaine, G., & Wesemael, F. 1995a, *ApJS*, 99, 189
- Chayer, P., Vennes, S., Pradhan, A. K., et al. 1995b, *ApJ*, 454, 429
- Di Stefano, R., Voss, R., & Claeys, J. S. W. 2011, *ApJL*, 738, L1
- Dilday, B., Howell, D. A., Cenko, S. B., et al. 2012, *Science*, 337, 942
- Dong, S., Katz, B., Kushnir, D., & Prieto, J. L. 2015, *MNRAS*, 454, L61
- Dong, S., Katz, B., Kollmeier, J. A., et al. 2018, *MNRAS*, 1805.00010
- Dupuis, J., Fontaine, G., Pelletier, C., & Wesemael, F. 1992, *ApJS*, 82, 505
- Eggleton, P. P. 1983, *ApJ*, 268, 368
- Fenn, D., Plewa, T., & Gawryszczak, A. 2016, *MNRAS*, 462, 2486
- Fink, M., Röpke, F. K., Hillebrandt, W., et al. 2010, *A&A*, 514, A53
- Fryxell, B., Olson, K., Ricker, P., et al. 2000, *ApJS*, 131, 273
- . 2010, FLASH: Adaptive Mesh Hydrodynamics Code for Modeling Astrophysical Thermonuclear Flashes, Astrophysics Source Code Library, ascl:1010.082
- Guillochon, J., Dan, M., Ramirez-Ruiz, E., & Rosswog, S. 2010, *ApJL*, 709, L64
- Hachisu, I., Kato, M., & Nomoto, K. 2012, *ApJL*, 756, L4
- Hawley, W. P., Athanassiadou, T., & Timmes, F. X. 2012, *ApJ*, 759, 39
- Iben, Jr., I., Nomoto, K., Tornambe, A., & Tutukov, A. V. 1987, *ApJ*, 317, 717
- Iben, Jr., I., & Tutukov, A. V. 1984, *ApJS*, 54, 335
- . 1985, *ApJS*, 58, 661
- . 1991, *ApJ*, 370, 615

- Iwasawa, M., Tanikawa, A., Hosono, N., et al. 2016, PASJ, 68, 54
- Jha, S., Branch, D., Chornock, R., et al. 2006, AJ, 132, 189
- Jiang, J.-A., Doi, M., Maeda, K., et al. 2017, Nature, 550, 80
- Justham, S. 2011, ApJL, 730, L34
- Kashi, A., & Soker, N. 2011, MNRAS, 417, 1466
- Kashyap, R., Fisher, R., García-Berro, E., et al. 2015, ApJL, 800, L7
- . 2017, ApJ, 840, 16
- Katz, B., & Dong, S. 2012, ArXiv e-prints, arXiv:1211.4584
- Kawai, Y., Saio, H., & Nomoto, K. 1988, ApJ, 328, 207
- Kawana, K., Tanikawa, A., & Yoshida, N. 2018, MNRAS, 477, 3449
- Kelly, P. L., Fox, O. D., Filippenko, A. V., et al. 2014, ApJ, 790, 3
- Kozma, C., Fransson, C., Hillebrandt, W., et al. 2005, A&A, 437, 983
- Kromer, M., Pakmor, R., Taubenberger, S., et al. 2013, ApJL, 778, L18
- Kromer, M., Fremling, C., Pakmor, R., et al. 2016, MNRAS, 459, 4428
- Krumholz, M. R., McKee, C. F., & Klein, R. I. 2006, ApJ, 638, 369
- Leung, S.-C., & Nomoto, K. 2018, ApJ, 861, 143
- Li, W., Bloom, J. S., Podsiadlowski, P., et al. 2011, Nature, 480, 348
- Litke, K. C., Chu, Y.-H., Holmes, A., et al. 2017, ApJ, 837, 111
- Liu, Z. W., Pakmor, R., Röpke, F. K., et al. 2012, A&A, 548, A2
- Liu, Z.-W., Pakmor, R., Seitzzahl, I. R., et al. 2013, ApJ, 774, 37
- Livne, E. 1990, ApJL, 354, L53
- Livne, E., & Glasner, A. S. 1990, ApJ, 361, 244
- Lorén-Aguilar, P., Isern, J., & García-Berro, E. 2010, MNRAS, 406, 2749
- Maeda, K., Jiang, J.-a., Shigeiyama, T., & Doi, M. 2018, ApJ, 861, 78
- Maeda, K., Taubenberger, S., Sollerman, J., et al. 2010, ApJ, 708, 1703
- Maeda, K., Leloudas, G., Taubenberger, S., et al. 2011, MNRAS, 413, 3075
- Maoz, D., Mannucci, F., & Nelemans, G. 2014, ARA&A, 52, 107
- Marion, G. H., Brown, P. J., Vinkó, J., et al. 2016, ApJ, 820, 92
- Meech, K. J., Weryk, R., Micheli, M., et al. 2017, Nature, 552, 378
- Namekata, D., Iwasawa, M., Nitadori, K., et al. 2018, PASJ, 70, 70
- Nomoto, K. 1982, ApJ, 257, 780
- Nomoto, K., & Leung, S.-C. 2018, SSRv, 214, 67
- Pakmor, R., Kromer, M., Röpke, F. K., et al. 2010, Nature, 463, 61
- Pakmor, R., Kromer, M., Taubenberger, S., & Springel, V. 2013, ApJL, 770, L8
- Pakmor, R., Röpke, F. K., Weiss, A., & Hillebrandt, W. 2008, A&A, 489, 943
- Papish, O., Soker, N., García-Berro, E., & Aznar-Siguán, G. 2015, MNRAS, 449, 942
- Paquette, C., Pelletier, C., Fontaine, G., & Michaud, G. 1986, ApJS, 61, 197
- Phillips, M. M., Li, W., Frieman, J. A., et al. 2007, PASP, 119, 360
- Raddi, R., Hollands, M. A., Gansicke, B. T., et al. 2018a, MNRAS, 479, L96
- Raddi, R., Hollands, M. A., Koester, D., et al. 2018b, ApJ, 858, 3
- Raskin, C., Scannapieco, E., Rockefeller, G., et al. 2010, ApJ, 724, 111
- Raskin, C., Timmes, F. X., Scannapieco, E., Diehl, S., & Fryer, C. 2009, MNRAS, 399, L156
- Rosswog, S., Kasen, D., Guillochon, J., & Ramirez-Ruiz, E. 2009, ApJL, 705, L128
- Sato, Y., Nakasato, N., Tanikawa, A., et al. 2015, ApJ, 807, 105
- . 2016, ApJ, 821, 67
- Schaefer, B. E., & Pagnotta, A. 2012, Nature, 481, 164
- Seitzzahl, I. R., Ciaraldi-Schoolmann, F., Röpke, F. K., et al. 2013, MNRAS, 429, 1156
- Shappee, B. J., Piro, A. L., Stanek, K. Z., et al. 2018, ApJ, 855, 6
- Shen, K. J., & Moore, K. 2014, ApJ, 797, 46
- Shen, K. J., & Schwab, J. 2017, ApJ, 834, 180
- Shen, K. J., Boubert, D., Gansicke, B. T., et al. 2018, ArXiv e-prints, 1804.11163
- Tanikawa, A. 2018a, ApJ, 858, 26
- . 2018b, MNRAS, 475, L67
- Tanikawa, A., Nakasato, N., Sato, Y., et al. 2015, ApJ, 807, 40
- Tanikawa, A., Sato, Y., Nomoto, K., et al. 2017, ApJ, 839, 81
- Tanikawa, A., Suzuki, T. K., & Doi, Y. 2018, PASJ, 70, 80
- Tanikawa, A., Yoshikawa, K., Nitadori, K., & Okamoto, T. 2013, NewA, 19, 74
- Tanikawa, A., Yoshikawa, K., Okamoto, T., & Nitadori, K. 2012, NewA, 17, 82

- Taubenberger, S., Kromer, M., Pakmor, R., et al. 2013, ApJL, 775, L43
- Timmes, F. X., Hoffman, R. D., & Woosley, S. E. 2000, ApJS, 129, 377
- Timmes, F. X., & Swesty, F. D. 2000, ApJS, 126, 501
- Vennes, S., Nemeth, P., Kawka, A., et al. 2017, Science, 357, 680
- Wang, B., Justham, S., & Han, Z. 2013, A&A, 559, A94
- Webbink, R. F. 1984, ApJ, 277, 355
- Woosley, S. E., & Kasen, D. 2011, ApJ, 734, 38
- Woosley, S. E., Taam, R. E., & Weaver, T. A. 1986, ApJ, 301, 601
- Woosley, S. E., & Weaver, T. A. 1994, ApJ, 423, 371
- Zenati, Y., Toonen, S., & Perets, H. B. 2018, ArXiv e-prints, arXiv:1803.04444